

# Observational Constraints on the Stellar Radiation Field Impinging on Transitional Disk Atmospheres

Judit Szulágyi

*Space Telescope Science Institute, 3700 San Martin Drive, Baltimore, MD 21218*

*Konkoly Observatory, Research Centre for Astronomy and Earth Sciences, Hungarian*

*Academy of Sciences, Konkoly Thege Miklós út 15-17, H-1121 Budapest, Hungary*

*Department of Astronomy, Eötvös Loránd University, Pázmány Péter sétány 1/a, H-1117*

*Budapest, Hungary*

szulagyi@konkoly.hu

Ilaria Pascucci

*Lunar and Planetary Laboratory, University of Arizona, 1629 East University Boulevard,*

*Tucson, AZ 85721*

Péter Ábrahám

*Konkoly Observatory, Research Centre for Astronomy and Earth Sciences, Hungarian*

*Academy of Sciences, Konkoly Thege Miklós út 15-17, H-1121 Budapest, Hungary*

Dániel Apai

*Department of Astronomy, The University of Arizona, 933 N Cherry Avenue, Tucson, AZ*

*85721*

Jeroen Bouwman

*Max Planck Institute for Astronomy, Königstuhl 17, D-69117 Heidelberg, Germany*

and

Attila Moór

*Konkoly Observatory, Research Centre for Astronomy and Earth Sciences, Hungarian  
Academy of Sciences, Konkoly Thege Miklós út 15-17, H-1121 Budapest, Hungary*

Received \_\_\_\_\_;    accepted \_\_\_\_\_

## ABSTRACT

Mid-infrared atomic and ionic line ratios measured in spectra of pre-main sequence stars are sensitive indicators of the hardness of the radiation field impinging on the disk surface. We present a low-resolution Spitzer IRS search for [Ar II] at  $6.98\,\mu\text{m}$ , [Ne II] at  $12.81\,\mu\text{m}$ , and [Ne III]  $15.55\,\mu\text{m}$  lines in 56 transitional disks. These objects, characterized by reduced near-infrared but strong far-infrared excess emission, are ideal targets to set constraints on the stellar radiation field onto the disk because their spectra are not contaminated by shock emission from jets/outflows or by molecular emission lines. After demonstrating that we can detect [Ne II] lines and recover their fluxes from the low-resolution spectra, here we report the first detections of [Ar II] lines towards protoplanetary disks. We did not detect [Ne III] emission in any of our sources. Our [Ne II]/[Ne III] line flux ratios combined with literature data suggest that a soft-EUV or X-ray spectrum produces these gas lines. Furthermore, the [Ar II]/[Ne II] line flux ratios point to a soft X-ray and/or soft-EUV stellar spectrum as the ionization source of the [Ar II] and [Ne II] emitting layer of the disk. If the soft X-ray component dominates over the EUV than we would expect larger photoevaporation rates hence a reduction of the time available to form planets.

*Subject headings:* circumstellar matter – infrared: stars – planetary systems: protoplanetary disks – stars: pre-main-sequence

## 1. Introduction

Young stars are often surrounded by circumstellar disks containing gas and dust. Most of the disk material is in the form of gas, while the dust component constitutes only a small fraction of the disk mass (e.g. Pascucci & Tachibana 2010). These circumstellar disks are planet nurseries; they provide the raw material for planets to form. Thus, understanding their evolution, especially the evolution of the gas component, is key to the understanding of planet formation.

The challenge in tracing the gaseous disk component is that the emission and excitation of gas species are very sensitive to chemical abundances, disk temperature, gas density and radiation field. Hence, multiple transitions at different wavelengths are necessary to probe a range of disk radii as well as of disk heights. As an example, the cold ( $T \simeq 50$  K) outer ( $> 100$  AU) disk is usually probed via CO sub-mm pure rotational lines (e.g. Dutrey et al. 2007) while observations of CO rovibrational lines in the near-infrared can be used to trace the hot ( $\sim 1,000$  K) gas within  $\sim 1$  AU from the central star (Najita et al. 2007a).

Intermediate disk radii where terrestrial and giant planets form have been probed only recently via new mid-infrared (mid-IR) gas lines discovered with the sensitive IRS spectrograph on board the *Spitzer Space Telescope* (e.g. Pascucci et al. 2007; Carr & Najita 2008; Salyk et al. 2008). One of the gas lines with a high detection rate in Spitzer spectra of young stars is the [Ne II] line at  $12.81\mu\text{m}$ . While this line likely probes shocked gas in an outflow from young star-disk systems with high accretion rates (Guedel et al. 2010; van Boekel et al. 2009), the same line is found to trace the hot ( $\geq 1,000$  K) disk atmosphere at several AU from sun-like stars that do not have fast (i.e.  $\sim 100$  km/s) outflows (Pascucci & Sterzik 2009; Najita et al. 2009; Sacco et al. 2012). Hence, the [Ne II] line at  $12.81\mu\text{m}$  provides a unique diagnostic to study the region of the disk that is exposed to high energy stellar photons from the central star (Glassgold et al. 2007;

Gorti & Hollenbach 2008; Hollenbach & Gorti 2009; Ercolano & Owen 2010). Because this hot atmosphere can become unbound at large disk radii, [Ne II] lines can be also used to test disk dispersal mechanisms such as photoevaporation driven by the central star (Alexander 2008; Pascucci & Sterzik 2009; Pascucci et al. 2011).

An interesting class of protoplanetary disks that might reveal how disks disperse their gas and dust is that of the so-called transitional disks (e.g. Strom et al. 1989). These objects display small near-IR but large far-IR excesses pointing to an optically thin inner cavity within the dust disk, believed to mark the disappearance of the primordial massive disk. Such inner cavities could be due to grain growth accompanying terrestrial planet formation, photoevaporation, dynamical clearing by a giant planet or a combination of these processes (e.g., Armitage 2011).

Recently, *Spitzer* high-resolution mid-infrared spectra of transitional disks have been discussed in the literature. In contrast to classical protoplanetary disks whose mid-IR spectra are dominated by molecular emission lines, especially of water (Carr & Najita 2008), the spectra of transitional disks present weak molecular lines but strong atomic and ionic emission lines (e.g. from [Ne II], Najita et al. 2010; Pontoppidan et al. 2010). In addition, transitional disks do not have signs of outflow activity pointing to a disk origin for most of the mid-infrared lines detected in their spectra. In summary, the lack of strong molecular lines and outflow activity make transitional disks ideal targets for detecting and analyzing additional atomic/ionic lines that could trace disk gas even using the low-resolution (hereafter LR with  $\lambda/\Delta\lambda \sim 60$ -120) IRS spectrograph on the *Spitzer Space Telescope*.

A very interesting ionic line that cannot be accessed with the high-resolution (hereafter HR with  $\lambda/\Delta\lambda \sim 600$ ) IRS module is the [Ar II] line at  $6.98\mu\text{m}$ . According to recent theoretical disk models (Hollenbach & Gorti 2009), the [Ar II] line luminosity should be

similar to that of the [Ne II] line in a disk irradiated by stellar EUV ( $13.6 \text{ eV} < h\nu \lesssim 100 \text{ eV}$ ) and X-ray ( $0.1\text{--}2 \text{ keV}$ ) photons. In addition, the [Ar II]/[Ne II] and [Ne II]/[Ne III] line ratios could help discriminate between cases in which a hard EUV, or a soft EUV or X-ray stellar spectrum<sup>1</sup> provide the main source of ionization for the disk atmosphere. The [Ar III] line at  $8.99 \mu\text{m}$  could be another important diagnostic of the stellar radiation field impinging on the disk and it is often detected in ionized gas surrounding massive stars (H II regions) together with [Ne II] and [Ar II] lines (e.g., Martín-Hernández et al. 2002). However, this line falls within the strong, broad, and common  $10 \mu\text{m}$  silicate emission feature also arising from the disk surface and it is expected to be weaker (by about a factor of 5, Hollenbach & Gorti 2009) than the [Ne II] and [Ar II] lines. Therefore, we have not attempted to recover this line in these low-resolution spectra. Constraining the main source of disk heating and ionization is necessary for properly estimating the rate at which disk gas is photoevaporated and hence the predicted disk lifetime. For instance, if photoevaporation is induced solely by EUV photons then photoevaporation rates are expected to be very low, of the order of  $\sim 10^{-10} \text{M}_{\odot} \text{yr}^{-1}$  (Alexander et al. 2004). Stellar X-rays can penetrate much larger columns of gas than EUV photons resulting in higher photoevaporation rates, up to two orders of magnitude higher than EUV-induced photoevaporation (Gorti et al. 2009; Owen et al. 2010). In this paper, we conduct a *Spitzer*-based search for [Ar II]  $6.98 \mu\text{m}$ , [Ne II]  $12.81 \mu\text{m}$ , and [Ne III]  $15.5 \mu\text{m}$  lines in a large sample of transitional disks. The resulting line ratios are compared to models of disks irradiated by high-energy stellar EUV

---

<sup>1</sup>A “hard” spectrum is that in which there are more photons at higher energies beyond a certain energy value. A hard X-ray spectrum is that in which there is substantial contribution from photons at and beyond  $1 \text{ keV}$ , while a hard EUV spectrum is that in which there are more photons with energies above  $41 \text{ eV}$  than below this value (for instance the often assumed power law  $\nu^{-1}$  for the EUV luminosity but also a black body with temperature  $\geq 35,000 \text{ K}$ ).

and X-ray photons to constrain the radiation field reaching the disk atmosphere.

## 2. Sample Selection and Data Reduction

We collected a comprehensive sample of disks from the literature that have lower near-, to mid-IR excess emission than classical protoplanetary disks. This sample includes classical transitional disks, cold disks, pre-transitional disks, and anemic disks<sup>2</sup>. In the following we will use the term transitional disks to refer to this sample of objects. We collected all available archival *Spitzer* IRS spectra for our sample. Since our main goal was to detect the [Ar II] line at 6.98  $\mu\text{m}$  and the [Ne II] line at 12.81  $\mu\text{m}$ , we focused on the Short Low (SL) module of the *Spitzer* IRS spectrograph, which covers the wavelength region between 5.2 and 14.5  $\mu\text{m}$ . However, when available we also reduced Long Low (LL) spectra to search for the [Ne III] line at 15.55  $\mu\text{m}$ . Based on the post-BCD processing, we excluded spectra from the sample that had poor signal-to-noise, or were contaminated by the spectrum of a nearby source, or the source was not detected in the SL module. Our final sample contains 56 objects covering an age range of 1-10 Myr, which are listed in Table 1 together with their classification and observation log.

Our data reduction started from the droopres intermediate data products obtained via processing of the raw IRS LR data with the SSC pipeline S18.7.0. Further processing was done with the spectral reduction tools developed for the Formation and Evolution of Planetary Systems (FEPS) *Spitzer* Legacy program (Meyer et al. 2004; Bouwman et al. 2008). In brief, the pairs of imaged spectra acquired along the spatial direction of the slit were subtracted from each other in order to correct for the background emission and stray light. Then, bad pixels were replaced with an interpolated value obtained from

---

<sup>2</sup><http://www.ipac.caltech.edu/spitzer2008/talks/Diskionary.pdf>

neighboring good pixels. Finally, the spectra were extracted from the background-subtracted pixel-corrected images using a 6.0 pixel and 5.0 pixel fixed-width aperture in the spatial dimension for the observations with the SL and LL modules, respectively. The spectra were calibrated using a spectral response function derived from multiple IRS spectra of the calibration star  $\eta^1$  Doradus and a MARCS stellar model provided by the Spitzer Science Center. Internal uncertainties per pixel were estimated by the FEPS pipeline as the standard deviation of the repeated spectral observations (i.e. for all slit positions and cycles, see details in Carpenter et al. 2008).

In order to identify [Ne II], [Ne III] and [Ar II] lines and to measure line fluxes, we used a robust, Monte-Carlo based Gaussian fitting method with IDL. In the case of [Ne II] lines, we fitted simultaneously a Gaussian to the line and a local parabola to the continuum (see Figure 1). We allowed at most a centroid shift of  $0.013 \mu\text{m}$  (roughly 20% of the wavelength spacing) to account for the wavelength calibration uncertainty in the SL1 module (IRS Instrument Handbook v.4 <sup>3</sup>). Because at the low-resolution of Spitzer ( $>2,000 \text{ km/s}$ ) lines from disks and even from jets/outflows are unresolved we further fixed the Gaussian width to  $0.043 \pm 0.008 \mu\text{m}$ , which is the value and uncertainty we determined from fitting 7 strong and unresolved [Ne II] lines in different supernova remnant LR Spitzer spectra. For the Monte-Carlo approach, we generated 1000 spectra within the range of a Gaussian distribution with a sigma equal to the uncertainty at each wavelength. For all of the spectra we repeated the fitting method and computed the area of the Gaussian. We used the mean of the line fluxes as final line flux and the standard deviation of the generated line fluxes as the uncertainty over the final line flux (see Pascucci et al. 2008 and Banzatti et al. 2012 for a similar method applied to silicate emission features and gas lines).

In the case of the [Ar II] line the adjacent intervals were too noisy for a simple Gaussian

---

<sup>3</sup><http://irsa.ipac.caltech.edu/data/SPITZER/docs/irs/irsinstrumenthandbook/>



fit. Thus, here we first subtracted a continuum with the following approach. We produced a median spectrum for each object which had multiple IRS LR spectra, in order to identify common lines and bands in the SL2 module (5.13-7.60  $\mu\text{m}$ ). Then, excluding these lines and bands we fitted a robust smooth curve to this module. We added in quadrature the continuum subtraction uncertainty to the original uncertainty on each datapoints. After, we followed the method described above for the [Ne II] lines to determine the line flux and uncertainty (see Figure 2). Here, the allowed centroid shifts were 0.008  $\mu\text{m}$  (roughly 20% of the wavelength spacing) which is the wavelength calibration uncertainty for the SL2 module (IRS Instrument Handbook v.4). The Gaussian width parameter was fixed to  $0.0241 \pm 0.0041$   $\mu\text{m}$  since this is the width and uncertainty of unresolved [Ar II] lines we measured from supernova remnant spectra as done for the [Ne II] lines.

When no line was detected, we computed  $3\sigma$  upper limits with the following equation:

$$F_{up} = 3Rd_{\lambda}\sqrt{N} \quad (1)$$

where  $R$  is the RMS of the data points around the line, and the line flux is computed over the resolution element ( $N = 2$  pixels), assuming the noise is uncorrelated. Here,  $d_{\lambda}$  is the wavelength of the given line divided by the resolution (fixed to 120). Along with the measured fluxes, the upper limits are in Table 2.

As a check to the absolute flux calibration, we integrated the IRS spectrum in the IRAC 8  $\mu\text{m}$  filter band and compared the integrated IRS flux to non-contemporaneous IRAC fluxes from the literature. Among the 31 objects that have IRAC fluxes, 42% showed less than 10% difference and 55% showed less than 20% difference. The absolute flux calibration accuracy is  $\sim 10\%$ , because we did not correct the flux for the location of the source in the slit (Swain et al. 2008). That about half of the objects present differences in fluxes larger than 20% is likely due to intrinsic infrared variability. Espaillat et al. (2011) found that the infrared spectral energy distributions (SEDs) of 8 out of 14 pre-

and classical–transitional disks vary by more than 20% on a timescale of years, consistent with our IRS–IRAC flux comparison. Because the [Ar II] and [Ne II] lines fall on different segments of the SL module, we performed additional tests to make sure that mispointing would not affect the line flux ratio. First of all, we checked that the SL and LL (when available) spectra match to within 10%. In addition, based on the difference in fluxes at overlapping wavelengths between the SL1, SL2, and SL3 modules we found that we would need to apply only small offsets in the source location within the slit to obtain the best match between these modules. These offsets do not affect line fluxes within the error bars we report here. As a demonstration of this, we applied these small offsets to four objects that have both [Ar II] and [Ne II] emissions in their spectra (TW Hya, CS Cha, 16201-2410, [PZ99]J160421.7-213028, see Sicilia-Aguilar et al. 2009 for the procedure). We could verify that the line fluxes (and hence their ratios) reported without applying any offset is the same as with applying the offsets within the uncertainties that we assign.

### 3. Results

Although the LR module has a spectral resolution that is 5 times lower than that of the HR module, strong mid-IR lines can be recovered in LR spectra of protoplanetary disks as demonstrated by Pascucci et al. (2009) for the HCN and C<sub>2</sub>H<sub>2</sub> rotation-vibration bands and in the following study by Teske et al. (2011). Here, we demonstrate that even atomic lines can be recovered in LR spectra of transitional disks. Figure 3 presents the TW Hya high-resolution SH2 spectrum (Najita et al. 2010) and our LR spectrum around the [Ne II] 12.81  $\mu$ m emission line of the same object. The comparison of the two spectra shows that the strongest lines in the HR module, the H I (7-6) line at 12.37  $\mu$ m and the [Ne II] line at 12.81  $\mu$ m, are also detected in the SL module. In addition, we show that the flux can be also recovered in LR spectra. The [Ne II] line flux measured in the LR

spectrum is  $(5.8 \pm 0.8) \times 10^{-14} \text{ erg s}^{-1} \text{ cm}^{-2}$ , which agrees within the estimated error bar with the flux from the HR SH2 spectrum:  $(5.56 \pm_{0.61}^{0.34}) \times 10^{-14} \text{ erg s}^{-1} \text{ cm}^{-2}$  (Najita et al. 2010). In addition to TW Hya, we also examined 9 other objects from our sample, which have available [Ne II] line fluxes in the literature (Guedel et al. 2010; Pascucci et al. 2007; Lahuis et al. 2007; Baldovin-Saavedra et al. 2011). We compared the fluxes from HR spectra to our LR flux values and we found that the fluxes are in good agreement within the associated error bars (see Figure 4).

We report here the first detections of [Ar II] lines in protoplanetary disks (Fig. 2). For the complete transitional disk sample, significance of each line detection is computed by dividing the line flux by its formal uncertainty (see Table 2). Two objects feature this line at a level  $>3\sigma$  and several others slightly below this threshold. Our detections prove that, in spite of their lower spectral resolution, the *Spitzer* LR spectra can be used to detect [Ar II] lines. [Ne II] lines are often detected in *Spitzer* HR spectra of disks (e.g. Pascucci et al. 2007; Lahuis et al. 2007; Guedel et al. 2010; Baldovin-Saavedra et al. 2011, see Table 3). We show here that detections are common even in LR spectra of transitional disks. In our sample [Ne II] emission appears in 17 objects with  $\geq 3\sigma$  level (see Fig. 1). Altogether one object from the total of 56 has both [Ar II] and [Ne II] gas lines in the same spectrum, counting only the  $\geq 3\sigma$  detections. In addition, one object shows only the [Ar II] line while 16 have only the [Ne II] line. We did not detect the [Ne III] line at  $15.5 \mu\text{m}$  in any of our objects, in agreement with the very few [Ne III] line detections in HR spectra in the literature. This shows that the [Ne III] line is typically weaker than the [Ne II] line even in transitional disks.

Because multiple *Spitzer*/IRS data reductions have been performed – e.g. Cornell Atlas of *Spitzer*/IRS Sources (hereafter Cassis, Leboutteiller et al. 2011) and SSC Enhanced

## Products <sup>4</sup>

When multiple observations of the same source were available, we found variability in the continuum and also in the intensity of the gas lines. There were multiple observations when we did not find a line that was however detected in most of the other spectra (e.g. GM Aur, see Fig. 1). We attribute variations by more than 20% to intrinsic source variability which was already observed in the mid-IR continuum and dust emission features of circumstellar disks (e.g. Muzerolle et al. 2009; Bary et al. 2009; Espaillat et al. 2011). Infrared variability is more likely a common characteristic of disks, especially of transitional disks (Espaillat et al. 2011). We emphasize however, that this variability does not significantly affect our analysis which focuses on flux ratios of lines belonging to the same mid-infrared spectrum.

In the simplest scenario in which ionization is carried out by EUV photons, the line flux ratio from two successive stages of ionization of a given element can be used to measure the slope of the spectral energy distribution (SED) of the ionizing field (e.g. Martín-Hernández et al. 2002). X-ray irradiation and ionization also produce different line ratios depending on the hardness of the X-ray spectrum. In the following we compute the  $[\text{Ne II}]/[\text{Ne III}]$  and  $[\text{Ne II}]/[\text{Ar II}]$  line flux ratios and analyze their distribution. The results will be compared with models from the literature in order to gain insight into the radiation field impinging on the disk surface.

---

<sup>4</sup><http://irsa.ipac.caltech.edu/data/SPITZER/docs/irs/irsinstrumenthandbook/84/> – we compared our reduced spectra with the products from those different pipelines. We downloaded the same observations (when they were available) and run our line detection routines on these spectra. We found, that the detections were the same (for  $[\text{Ne II}]$  and  $[\text{Ar II}]$  lines as well) regardless of the used reduction pipeline. Usually we got similar SNRs, see examples on Fig. 2).

### 3.1. [Ne II]/[Ne III] Line Flux Ratios

Because of the [Ne III] line non-detections in our LR spectra, we can only derive lower limits for [Ne II]/[Ne III] line ratios (see left panel on Figure 5). On Fig. 5 we also over-plot model predictions from: a hard EUV spectrum ( $L_\nu \propto \nu^{-1}$ ) in light gray, and a soft EUV (black body emission at  $T_{\text{eff}} = 30,000 \text{ K}$ )/X-ray irradiation in dark gray (Hollenbach & Gorti 2009). Expanding on the X-ray model predictions by Hollenbach & Gorti (2009), Ercolano & Owen (2010) simulated 3 different X-ray luminosity cases for primordial disks and various hole sizes for transitional disks. We note that in these models the hole is both in the gas and in the dust distribution while most transitional disks are not completely empty of gas in the dust hole as evinced by their on-going accretion. These model predictions are also plotted on Fig. 5 with light green slanted stripes for various X-ray luminosity models and light blue vertical stripes for various hole size models. In summary, all model predictions point to a [Ne II]/[Ne III] line ratio  $> 1$  for an impinging soft EUV spectrum and/or X-ray (hard or soft) spectrum.

Since all our data points are lower limits, they cannot unequivocally discriminate between hard EUV and X-ray/soft EUV models. However, several of our lower limits lie above the hard EUV limit, suggesting the dominance of the X-ray/soft EUV spectrum. In order to further analyze this question we collected [Ne II]/[Ne III] line flux ratios from the literature computed from HR IRS spectra (Table 3). Even with the HR module most [Ne III] lines are not detected. The exceptions are the [Ne III] lines from Sz 102, an object with a known jet (Lahuis et al. 2007), WL5/GY246 (Flaccomio et al. 2009), and a possible detection of this line from TW Hya (Najita et al. 2010). These lower limits and measurements from the literature on the right panel of Fig. 5 clearly favor an X-ray/soft EUV ionizing spectrum impinging on the disk. All [Ne II]/[Ne III] lower limits from the HR spectra are  $> 1$  and thus exclude that a hard EUV spectrum ionize neon atoms at the disk

surface. This result is in agreement with previous HR studies of smaller samples of disks (e.g. Pascucci et al. 2007; Lahuis et al. 2007).

### 3.2. [Ne II]/[Ar II] Line Flux Ratios

Figure 6 shows the distribution of the computed [Ne II]/[Ar II] line flux ratios for our sample of transitional disks. The dataset contains measured values, lower limits and also one upper limit. On the same figure we also over-plot the hard X-ray and soft X-rays/EUV model predictions by Hollenbach & Gorti (2009) with darker gray and vertical light gray stripes, respectively. Their model uses solar Ne/Ar elemental abundance ratio. Due to the dominance of lower limits we cannot discriminate between the models. However the distribution of the data, in particular the measured flux ratios, cluster closer to the  $\sim 1$  which points to the soft X-ray/EUV case.

We also computed the median of continuum-subtracted and distance-corrected spectra for [Ne II] line detections and found a median flux value of  $1.49 \times 10^{-14}$  erg s $^{-1}$  cm $^{-2}$  at the distance of the Taurus star-forming region (140 pc). In the case of the [Ar II] line, where we have only 2 firm detections, the fluxes at the Taurus distance are 1.81 and  $5.90 \times 10^{-14}$  erg s $^{-1}$  cm $^{-2}$ .

Our sample is dominated by [Ne II]/[Ar II] line ratio lower limits, hence we perform further analysis to identify what is the typical line flux ratio for the sample. In order to compute the representative line ratio values for the distribution, we applied survival analysis with the software package “Astronomy SURVival Analysis” (ASURV, Isobe & Feigelson 1990; Lavalley et al. 1992; Feigelson & Nelson 1985). We chose this statistical method due to the many lower limits in the flux ratio data. Survival analysis can provide a cumulative distribution function of a given sample containing measured data points and censored

data points as well. From the distribution, this method can also estimate a mean value of the distribution. Among the ASURV different subroutines, we applied a Kaplan-Meier estimator, which is a self-consistent, generalized maximum-likelihood estimator for the population from which the sample was drawn. The ASURV code can handle only right or left censored data (only lower or upper limits respectively), but cannot do both at the same time. Therefore we applied the analysis on  $[\text{Ne II}]/[\text{Ar II}]$  line ratio lower limits and measured data points. As a result, the mean is equal to  $1.20 \pm 0.06$ . This value is below the hard X-ray stellar spectrum model hinting to the soft X-ray and EUV spectrum model. Although, given that the majority of the  $[\text{Ne II}]/[\text{Ar II}]$  line ratios are lower limits, one cannot unequivocally rule out the hard X-ray model either.

#### 4. Discussion

Emission from ionized atoms, such as  $\text{Ne}^+$ ,  $\text{Ne}^{++}$ , and  $\text{Ar}^+$ , can be produced either in the interstellar medium gas that is shocked by protostellar winds or in the low-mass-disk surface layer by gas that is heated and ionized by stellar high energy photons (Hollenbach & Gorti 2009; Ercolano & Owen 2010; Glassgold et al. 2007). A spectacular example of the first case is the T Tauri triple system where van Boekel et al. (2009) spatially and spectrally resolved the strong  $[\text{Ne II}]$  emission detected in Spitzer spectra. However, transitional disks, such as those in our sample, have no obvious signs of outflow activity suggesting that the unresolved emission lines in Spitzer spectra trace the disk surface. This has been confirmed at least in seven transitional disks observed at high spectral and spatial resolution with the VLT/VISIR spectrograph (Pascucci & Sterzik 2009; Sacco et al. 2012). The  $[\text{Ne II}]$  FWHMs are found to be relatively narrow (15-40 km/s) and to peak close to (but not exactly at) the stellar velocity. An outflow origin for this line would result in much broader profiles ( $\sim 100$  km/s) as well as more blueshifted peaks ( $\sim -100$  km/s). Further

evidence that the [Ne II] emission in transitional disks arises primarily from the disk is provided by Guedel et al. (2010). They find that known outflow sources are remarkably separated from the other sources by having [Ne II] luminosities 1 to 2 orders of magnitude higher. These findings strongly support a disk origin for the [Ne II] emission detected toward transitional objects, and very likely for the [Ar II] lines as well. In the specific case of the transitional disk around TW Hya, the spectrally resolved [Ne II] line profiles demonstrate that most of the [Ne II] emission arises from the disk beyond the dust inner radius (Pascucci et al. 2011).

We turn now to model predictions of disks irradiated by EUV and X-ray photons to understand what our observations are telling us about the radiation impinging on the disk surface. Hollenbach & Gorti (2009) have shown analytically and with numerical models that a hard EUV ( $L_{EUV(\nu)} \propto \nu^{-1}$ ) spectrum produces more [Ne III] than [Ne II] emission. This stems from the fact that there are more high-energy (around 40 eV) than low-energy (around 21 eV) photons ionizing Ne atoms and  $\text{Ne}^+$  ions, as also found in HII regions when the stellar temperature of the massive star is  $\geq 35,000$  K. A higher [Ne III]/[Ne II] line flux ratio is clearly in contrast with observed ratios (see Sect. 3.1) thus excluding a hard EUV spectrum as the main source of ionization for neon atoms in the atmosphere of transitional disks. Because the detected [Ne II] lines are at least  $\sim 10$  times stronger than the [Ne III] lines, if they trace the EUV layer then the EUV spectrum impinging on the disk should be that created by a black body with effective temperature 30,000 K (the spectrum drops sharply from 21 eV to 40 eV which results in more low-energy photons, see Hollenbach & Gorti 2009). A disk irradiated solely by X-rays also produces more [Ne II] than [Ne III] emission (Glassgold et al. 2007), because of the rapid charge exchange reactions of  $\text{Ne}^{++}$  with atomic hydrogen. This [Ne II] over [Ne III] dominance is also in agreement with observations. Further modeling by Ercolano & Owen (2010) including both X-rays and EUV shows that this ratio is sensitive to the X-ray luminosity as well as



to the disk structure, transitional versus classical disks<sup>5</sup>. According to their model, the [Ne II]/[Ne III] line flux ratio ranges from  $\sim 3$  to  $\sim 5$  in disks with inner holes of different sizes from 8.5 AU to 30.5 AU. Moreover, this ratio ranges from  $\sim 5$  to  $\sim 9$  in primordial disks depending on various X-ray luminosities. In summary, the observed [Ne II]/[Ne III] line ratio could be produced either by a soft EUV, a soft X-ray, or a hard X-ray spectrum.

The first ionization potential of argon is 15.76 eV, lower than that of neon. Thus, the intensity of [Ar II] lines allows one to constrain the SED of the ionizing field at lower energies than what is possible with the [Ne II] and [Ne III] transitions. Hollenbach & Gorti (2009) predict the [Ar II] 6.98  $\mu\text{m}$  line to be one of the strongest forbidden lines arising from the hot disk atmosphere. More specifically, they predict a strength very similar to that of the [Ne II] 12.81  $\mu\text{m}$  line (assuming solar Ne/Ar elemental abundance ratio) when the heating is by EUV or soft X-rays and a factor of  $\sim 2.5$  weaker line when the heating is by hard X-rays (see also their Fig 4). This is mainly due to the fact that the X-ray heated gas is at a lower temperature, closer to that of the [Ne II] transition than to the much higher [Ar II] line. The line flux ratios measured in this work point to a soft EUV and/or soft X-ray spectrum producing the [Ne II] and [Ar II] lines in transitional disks. These soft emission spectra, in the EUV as well as in the X-ray regimes, are thought to be connected to the accretion of disk gas onto the central star. For instance, X-rays could arise in accretion shocks along the funnel connecting the circumstellar disk to the star (e.g. Kastner et al. 2002). Chromospheric EUV emission is known to have a power-law like spectrum (Ribas et al. 2005), thus it could contribute only marginally to the observed [Ne II] and [Ar II] emission lines. Based on the [Ne II] line median flux value and the [Ar II] line flux range reported in Sect. 3.2 and eq. 8 from Hollenbach & Gorti (2009), we

---

<sup>5</sup>A disk that is irradiated by EUV and X-rays will have a fully ionized HII-like region at 10,000 K on top of a hot, more neutral X-ray ( $\sim 1\,000$  K) layer.

also calculate that  $\sim 10^{41}$  photons/s are necessary to reproduce these fluxes for a EUV-only irradiation. If X-rays contribute or dominate, this number should be taken as an upper limit. We note that independent calculations of the stellar ionizing flux produced by young stars range from  $\sim 10^{40}$ – $10^{42}$  photons/s for the transitional disk around TW Hya (Herczeg et al. 2007; Pascucci et al. 2012) and to  $10^{41}$ – $10^{44}$  photons/s for classical T Tauri stars (Alexander et al. 2005). Hence, our results are in line with an [Ar II] emission also produced by the disk surface. The X-ray component that might dominate disk irradiation is especially exciting because X-rays can heat and ionize larger columns of gas than EUV and thus drive larger photoevaporative winds (Ercolano et al. 2009; Gorti & Hollenbach 2009). Models that include X-ray irradiation of the disk surface predict up to two orders of magnitude higher mass loss rates in comparison to EUV-only irradiated disks (Owen et al. 2010). Such high photoevaporation rates could dominate the evolution and dispersal of protoplanetary disks. Ongoing photoevaporation has been detected already in a few transitional disks (Pascucci & Sterzik 2009; Pascucci et al. 2011; Sacco et al. 2012).

More [Ar II] line detections are clearly necessary to expand upon these first and exploratory results. This study will be important for planning future and more sensitive MIR observations of disks. The spectrometer MIRI on the *James Webb Space Telescope* will be able to easily detect the ionic lines discussed here. According to current estimates MIRI will be able to detect a line flux of  $1 \times 10^{-19}$  W/m<sup>2</sup> at 7  $\mu$ m with a signal-to-noise of 10 in just 100 sec. This flux is about 60 times lower than our [Ar II] line fluxes corrected to the 140 pc distance of the Taurus star-forming region. With more [Ar II] detections it will be possible not only to better measure the [Ne II]/[Ar II] flux ratio in transitional disks but also to explore how line fluxes evolve with stellar and disk evolutionary stage thus constraining the time evolution of photoevaporation rates. Confirming that [Ar II] lines really trace photoevaporating gas requires much higher spectral and spatial resolution than that available with MIRI (only  $\sim 100$  km/s). EXES on *SOFIA* is perfectly suited for this

task. Although much less sensitive than MIRI, it is still sensitive enough to detect fluxes similar to our [Ar II] line fluxes, at the distance of Taurus. Its high resolution mode will provide up to  $R \sim 120,000$  or 2.5 km/s around 7  $\mu\text{m}$  enabling to spectrally resolve [Ar II] lines if they trace photoevaporating gas at tens of AU from the central star as predicted. The 3 signal-to-noise level will be reachable in 140 minutes for a resolved (10 bins) line. Our transitional disks with [Ar II] detections are the best targets for high-resolution follow-up studies of the gas kinematics with SOFIA.

## 5. Summary

In this paper we present [Ar II] and [Ne II] line detections in low-resolution (LR) *Spitzer*/IRS spectra. From the [Ne II]/[Ar II] and [Ne II]/[Ne III] line flux ratios, we investigate whether the ionization of the [Ne II], [Ne III] and [Ar II] emitting layer is mainly due to soft/hard X-rays or EUV photons impinging on the disk. Our results can be summarized as follows:

1. We report the first detections of [Ar II] lines in protoplanetary disks. We detected this line in 2 sources at a level  $>3\sigma$ , altogether 4% of the sample show [Ar II] detections.
2. We also detected [Ne II] lines for the first time in LR IRS spectra. Our 17 detections with at least  $3\sigma$  level account for 30% of the objects in our sample.
3. Our [Ne II]/[Ne III] line ratio when combined with literature data excludes that the layer emitting [Ne II] and [Ne III] is mostly ionized by a hard stellar EUV ( $L_{\text{EUV}(\nu)} \propto \nu^{-1}$ ) spectrum.
4. The [Ar II]/[Ne II] line flux ratios are dominated by lower limits, thus one cannot distinguish unambiguously between the two models. However, the distribution of the

upper/lower limits, as well as the measured values, seem to favor the soft X-rays/EUV stellar spectrum rather than a hard X-ray spectrum reaching the [Ar II] and [Ne II] emitting layer of the disk. Clearly, more [Ar II] line detections are needed to better constrain photoevaporative disk models.

A dominance of the soft X-ray component would point to larger photoevaporation rates than when photoevaporation is solely driven by EUV photons, which influences the lifetime and extension of dust gaps in transitional disks (Owen et al. 2011).

## 6. Acknowledgments

J. Sz. acknowledges support through the Spitzer Data Analysis grant 1348621 to I. Pascucci and D. Apai. This work was partly supported by the NASA/ADP grant NNX10AD62G and the grant OTKA K101393 of the Hungarian Scientific Research Fund. We thank to our referee, Dan Watson, for the very useful comments and suggestions, which significantly improved this manuscript. Furthermore, we are thankful to Uma Gorti, David Hollenbach, and Eric D. Feigelson for useful discussions.

*Facilities:* Spitzer Space Telescope (IRS).

## REFERENCES

- Alexander, R. D., Clarke, C. J., & Pringle, J. E., 2004, MNRAS, 348, 879
- Alexander, R. D., Clarke, C. J., & Pringle, J. E. 2005, MNRAS, 358, 283
- Alexander, R. D., 2008, MNRAS, 391, 64
- Armitage, P. J. 2011, ARA&A, 49, 195
- Baldovin-Saavedra, C., Audard, M., Güdel, M., et al. 2011, A&A, 528, A22
- Banzatti, A., Meyer, M. R., Bruderer, S., et al. 2012, ApJ, 745, 90
- Bary, J. S., Leisenring, J. M., & Skrutskie, M. F., 2009, ApJ, 706, 168
- Bouwman, J., Henning, Th., Hillenbrand, L. A., Meyer, M. R., Pascucci, I., Carpenter, J., Hines, D., Kim, J. S., Silverstone, M. D., Hollenbach, D., & Wolf, S., 2008, ApJ, 683, 479
- Brown, J. M., Blake, G. A., Dullemond, C. P., Merín, B., Augereau, J. C., Boogert, A. C. A., Evans, N. J., II, Geers, V. C., Lahuis, F., Kessler-Silacci, J. E., Pontoppidan, K. M., & van Dishoeck, E. F., 2007, ApJ, 664, 107
- Calvet, N., D’Alessio, P., Hartmann, L., Wilner, D., Walsh, A., & Sitko, M., 2002, ApJ, 568, 1008
- Carpenter, J. M., Bouwman, J., Silverstone, M. D., Kim, J. S., Stauffer, J., Cohen, M., Hines, D. C., Meyer, M. R., & Crockett, N., 2008, ApJS, 179, 423
- Carr, J. S., & Najita, J. R., 2008, Science, 319, 1504
- Cieza, L., Padgett, D. L., Stapelfeldt, K. R., Augereau, J.-C., Harvey, P., Evans, N. J., II, Merín, B., Koerner, D., Sargent, A., van Dishoeck, E. F., Allen, L., Blake, G.,

- Brooke, T., Chapman, N., Huard, T., Lai, S.-P., Mundy, L., Myers, P. C., Spiesman, W., & Wahhaj, Z., 2007, *ApJ*, 667, 308
- Dahm, S. E., & Carpenter, J. M., 2009, *AJ*, 137, 4024
- Dutrey, A., Guilloteau, S., & Ho P., 2007, *Protostars and Planets V*, ed. B. Reipurth, D. Jewitt, and K. Keil (Tucson: University of Arizona Press), 495
- Ercolano, B. Clarke, C. J., & Drake, J. J., 2009, *ApJ*, 699, 1639
- Ercolano, B. & Owen, J. E., 2010, *MNRAS*, 406, 1553
- Espaillat, C., Calvet, N., D’Alessio, P., Hernández, J., Qi, C., Hartmann, L., Furlan, E., & Watson, D. M., 2007, *ApJ*, 670, 135
- Espaillat, C., Muzerolle, J., Hernández, J., Briceño, C., Calvet, N., D’Alessio, P., McClure, M., Watson, D. M., Hartmann, L., & Sargent, B., 2008, *ApJ*, 689, 145
- Espaillat, C., Furlan, E., D’Alessio, P., Sargent, B., Nagel, E., Calvet, N., Watson, Dan M., & Muzerolle, J., 2011, *ApJ*, 728, 49
- Feigelson, E. D., & Nelson, P. I., 1985, *ApJ*, 293, 192
- Flaccomio, E., Stelzer, B., Sciortino, S., Micela, G., Pillitteri, I., & Testi, L., 2009, *A&A*, 505, 695
- Furlan, E., Sargent, B., Calvet, N., Forrest, W. J., D’Alessio, P., Hartmann, L., Watson, D. M., Green, J. D., Najita, J., & Chen, C. H., 2007, *ApJ*, 664, 1176
- Furlan, E., Watson, D. M., McClure, M. K., Manoj, P., Espaillat, C., D’Alessio, P., Calvet, N., Kim, K. H., Sargent, B. A., Forrest, W. J., & Hartmann, L., 2009, *ApJ*, 703, 1964

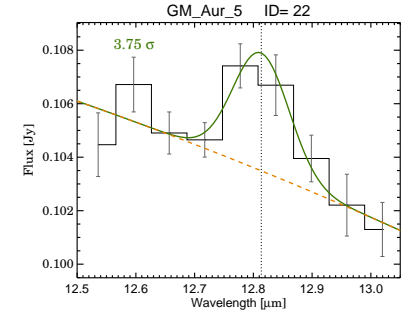
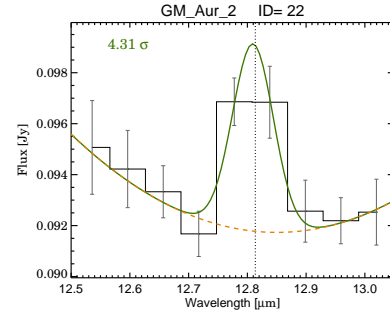
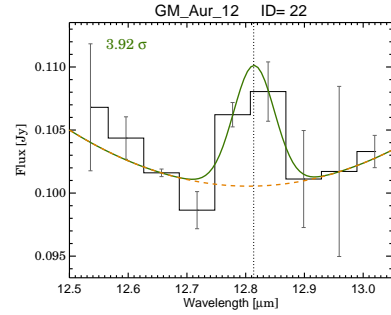
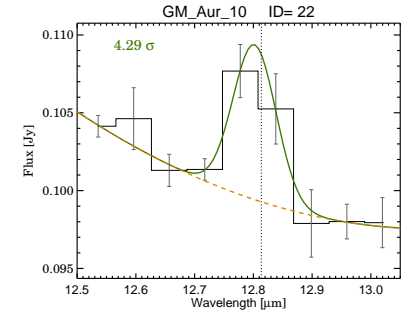
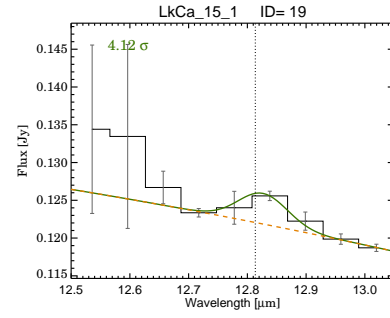
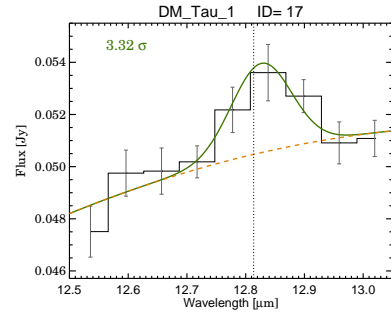
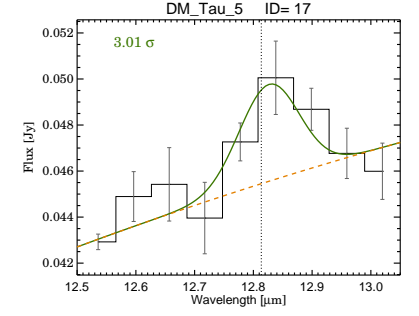
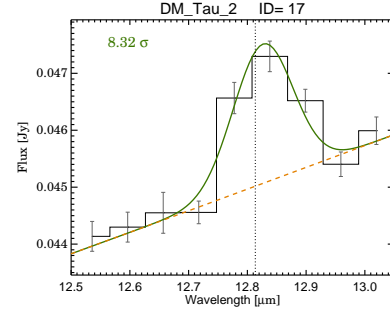
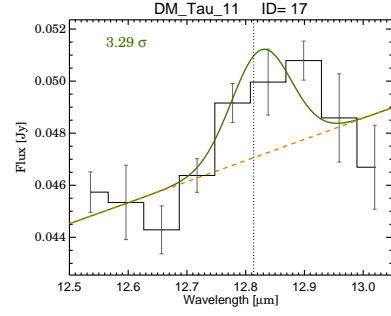
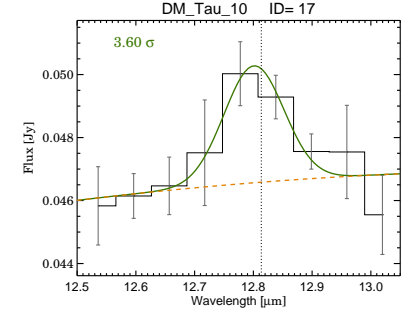
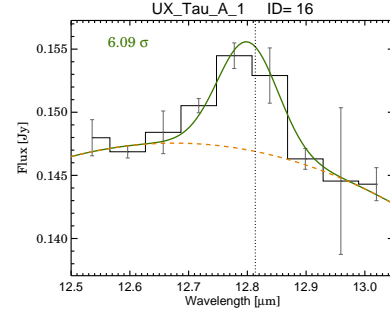
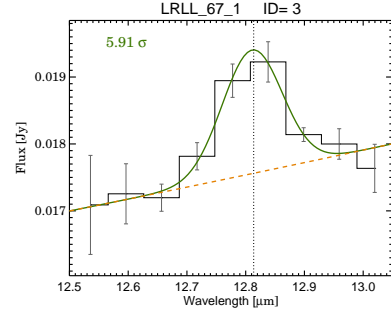
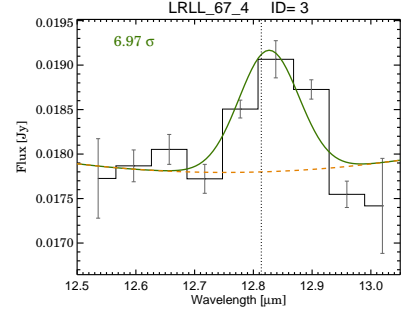
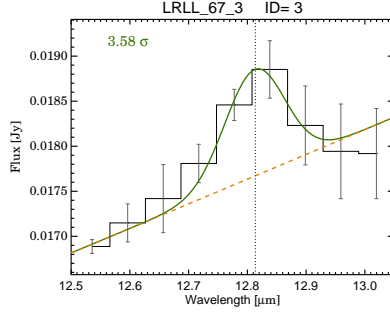
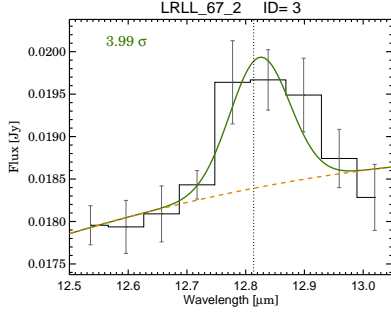
- Glassgold, A. E., Najita, J. R., & Igea, J., 2007, *ApJ*, 656, 515
- Gorti, U., & Hollenbach, D., 2008, *ApJ*, 683, 287
- Gorti, U., & Hollenbach, D., 2009, *ApJ*, 690, 1539
- Gorti, U., Dullemond, C. P., & Hollenbach, D. 2009, *ApJ*, 705, 1237
- Guedel, M., Lahuis, F., Briggs, K. R., Carr, J., Glassgold, A. E., Henning, Th., Najita, J. R., van Boekel, R., & van Dishoeck, E., 2010, *A&A*, 519, A113
- Herczeg, G. J., Najita, J. R., Hillenbrand, L. A., & Pascucci, I. 2007, *ApJ*, 670, 509
- Hollenbach, D. & Gorti, U., 2009, *ApJ*, 703, 1203
- Isobe, T., & Feigelson, E. D., 1990, *BAAS*, 22, 917
- Kastner, J. H., Huenemoerder, D. P., Schulz, N. S., Canizares, C. R., & Weintraub, D. A. 2002, *ApJ*, 567, 434
- Kim, K. H., Watson, D. M., Manoj, P., Furlan, E., Najita, J., Forrest, W. J., Sargent, B., Espaillat, C., Calvet, N., Luhman, K. L., McClure, M. K., Green, J. D., & Harrold, S. T., 2009, *ApJ*, 700, 1017
- Lahuis, F., van Dishoeck, E. F., Blake, G. A., Evans, N. J., II, Kessler-Silacci, J. E., & Pontoppidan, K. M., 2007, *ApJ*, 665, 492
- Lavalley, M. P., Isobe, T., & Feigelson, E. D., 1992, *BAAS*, 24, 839
- Lebouteiller, V., Barry, D. J., Spoon, H. W. W., et al. 2011, *ApJS*, 196, 8
- Luhman, K. L., Allen, L. E., Allen, P. R., Gutermuth, R. A., Hartmann, L., Mamajek, E. E., Megeath, S. T., Myers, P. C., & Fazio, G. G., 2008, *ApJ*, 675, 1375

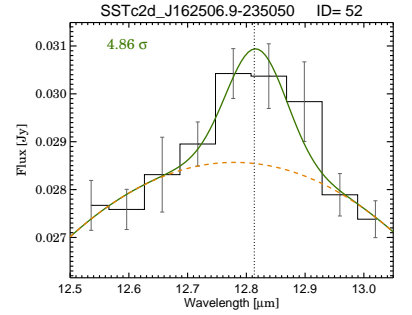
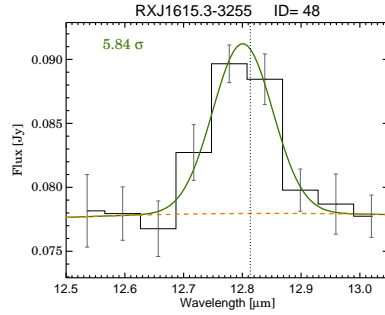
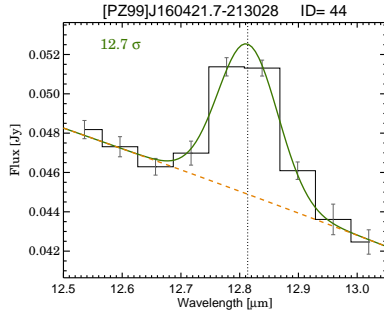
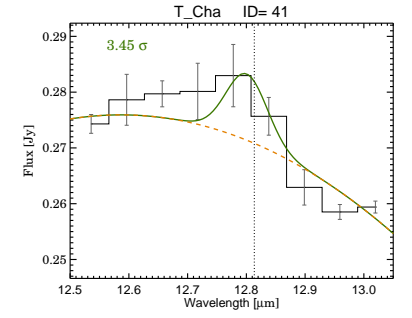
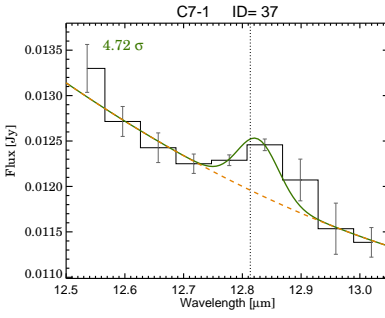
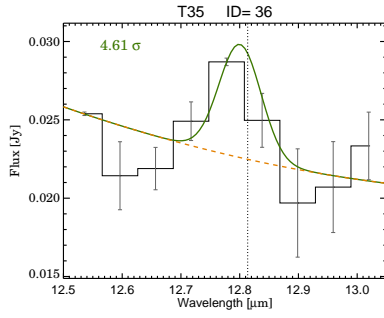
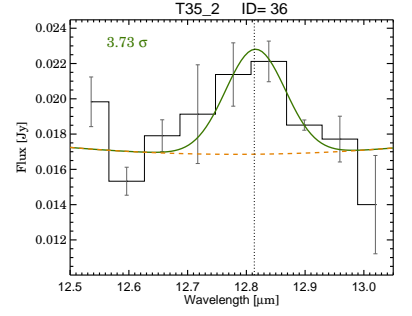
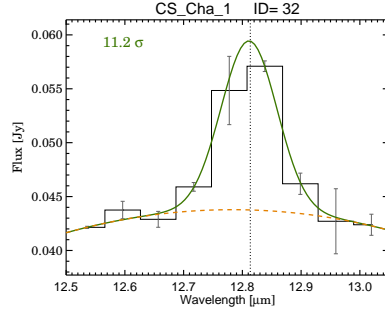
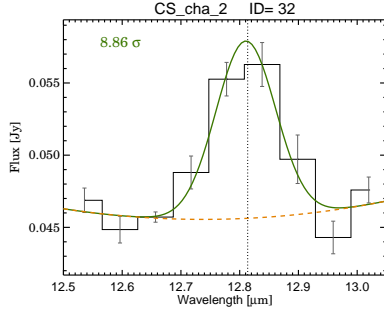
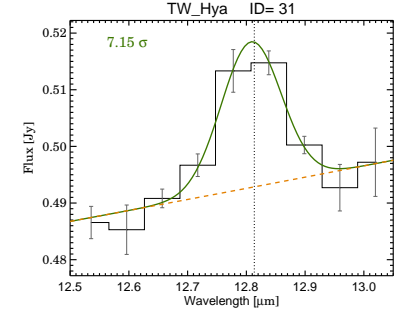
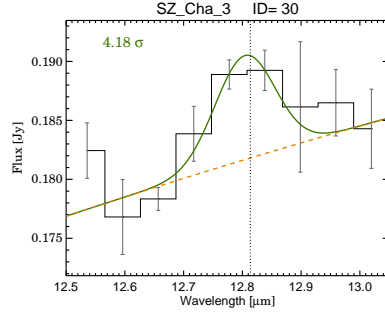
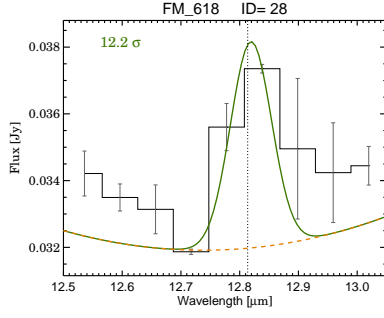
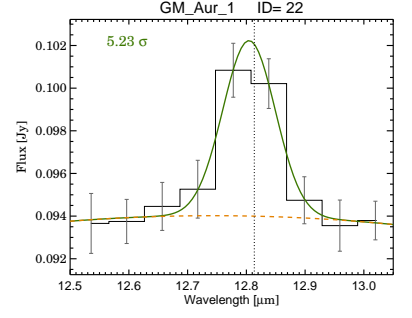
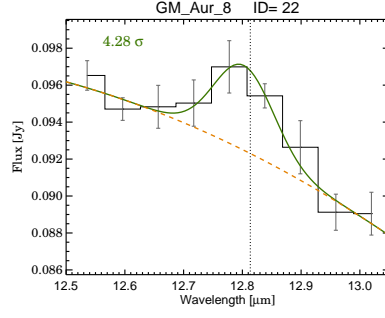
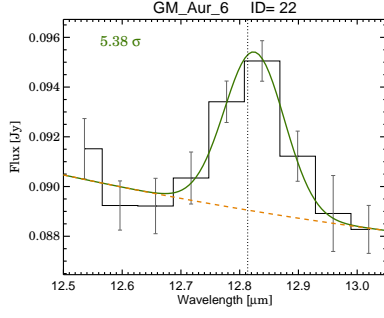
- Martín-Hernández, N. L., Peeters, E., Morisset, C., Tielens, A. G. G. M., Cox, P., Roelfsema, P. R., Baluteau, J.-P., Schaerer, D., Mathis, J. S., Damour, F., Churchwell, E., & Kessler, M. F., 2002, *A&A*, 381, 606
- Merín, B., Brown, J. M., Oliveira, I., Herczeg, G., van Dishoeck, E. F., Bottinelli, S., Pontoppidan, K. M., Evans, N. J., II, Cieza, L., Spezzi, L., Alcalá, J. M., Harvey, P. M., Blake, G. A., Bayo, A., Geers, V. G., Lahuis, F., Prusti, T., Augereau, J.-C., Olofsson, J., Walter, F. M., Chiu, K., 2010, *ApJ*, 718, 1200
- Meyer, M. R., Hillenbrand, L. A., Backman, D. E., Beckwith, S. V. W., Bouwman, J., Brooke, T. Y., Carpenter, J. M., Cohen, M., Gorti, U., Henning, T., Hines, D. C., Hollenbach, D., Kim, J. S., Lunine, J., Malhotra, R., Mamajek, E. E., Metchev, S., Moro-Martin, A., Morris, P., Najita, J., Padgett, D. L., Rodmann, J., Silverstone, M. D., Soderblom, D. R., Stauffer, J. R., Stobie, E. B., Strom, S. E., Watson, D. M., Weidenschilling, S. J., Wolf, S., Young, E., Engelbracht, C. W., Gordon, K. D., Misselt, K., Morrison, J., Muzerolle, J., & Su, K., 2004, *ApJS*, 154, 422
- Muzerolle, J., Flaherty, K., Balog, Z., Furlan, E., Smith, P. S., Allen, L., Calvet, N., D’Alessio, P., Megeath, S. T., Muench, A., Rieke, G. H., & Sherry, W. H., 2009, *ApJ*, 704, 15
- Muzerolle, J., Allen, L. E., Megeath, S. T., Hernández, J., Gutermuth, R. A., 2010, *ApJ*, 708, 1107
- Najita, J. R., Carr, J. S., Glassgold, A. E., & Valenti, J. A., 2007a, *Protostars and Planets V*, ed. B. Reipurth, D. Jewitt, and K. Keil (Tucson: University of Arizona Press), 507
- Najita, J. R., Strom, S. E., & Muzerolle, J., 2007b, *MNRAS*, 378, 369



- Najita, J. R., Doppmann, G. W., Bitner, M. A., Richter, M. J., Lacy, J. H., Jaffe, D. T., Carr, J. S., Meijerink, R., Blake, G. A., Herczeg, G. J., Glassgold, A. E., 2009, *ApJ*, 697, 957
- Najita, J. R., Carr, J. S., Strom, S. E., Watson, D. M., Pascucci, I., Hollenbach, D., Gorti, U., & Keller, L., 2010, *ApJ*, 712, 274
- Owen, J. E., Ercolano, B., Clarke, C. J., & Alexander, R. D., 2010, *MNRAS*, 401, 1415
- Owen, J. E., Ercolano, B., & Clarke, C. J. 2011, *MNRAS*, 412, 13
- Pascucci, I., Hollenbach, D., Najita, J., Muzerolle, J., Gorti, U., Herczeg, G. J., Hillenbrand, L. A., Kim, J. S., Carpenter, J. M., Meyer, M. R., Mamajek, E. E., & Bouwman, J., 2007, *ApJ*, 663, 383
- Pascucci, I., Apai, D., Hardegree-Ullman, E. E., et al. 2008, *ApJ*, 673, 477
- Pascucci, I., Apai, D., Luhman, K., Henning, Th., Bouwman, J., Meyer, M. R., Lahuis, F., & Natta, A., 2009, *ApJ*, 696, 143
- Pascucci, I., & Sterzik, M., 2009, *ApJ*, 702, 724
- Pascucci, I., & Tachibana, S., 2010, *Protoplanetary Dust: Astrophysical and Cosmochemical Perspectives*, 263
- Pascucci, I., Sterzik, M., Alexander, R. D., et al. 2011, *ApJ*, 736, 13
- Pascucci, I., Gorti, U., & Hollenbach, D. 2012, *ApJ*, 751, L42
- Pontoppidan, K. M., Salyk, C., Blake, G. A., Meijerink, R., Carr, J. S., & Najita, J., 2010, *ApJ*, 720, 887
- Ribas, I., Guinan, E. F., Güdel, M., & Audard, M. 2005, *ApJ*, 622, 680

- Sacco, G. G., Flaccomio, E., Pascucci, I., et al. 2012, *ApJ*, 747, 142
- Salyk, C., Pontoppidan, K. M., Blake, G. A., Lahuis, F., van Dishoeck, E. F., & Evans, N. J., II, 2008 *ApJ*, 676, 49
- Sicilia-Aguilar, A., Bouwman, J., Juhász, A., Henning, T., Roccatagliata, V., Lawson, W. A., Acke, B., Feigelson, E. D., Tielens, A. G. G. M., Decin, L., & Meeus, G., 2009, *ApJ*, 701, 1188
- Strom, K. M., Strom, S. E., Edwards, S., Cabrit, S., & Skrutskie, M. F. 1989, *AJ*, 97, 1451
- Swain, M. R., Bouwman, J., Akeson, R. L., Lawler, S., & Beichman, C. A. 2008, *ApJ*, 674, 482
- Teske, J. K., Najita, J. R., Carr, J. S., et al. 2011, *ApJ*, 734, 27
- van Boekel, R., Guedel, M., Henning, Th., Lahuis, F., & Pantin, E., 2009, *A&A*, 497, 137





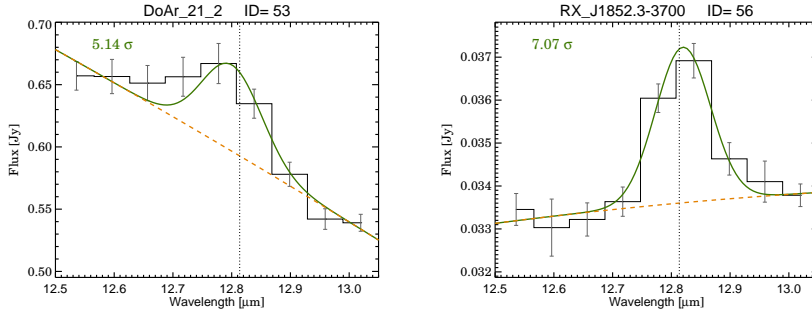


Fig. 1.— The [Ne II] line detections ( $\geq 3\sigma$ ) where green curves indicate the fitted Gaussians and orange curves mark the continuum. The corresponding SNR is plotted on the top left corner.

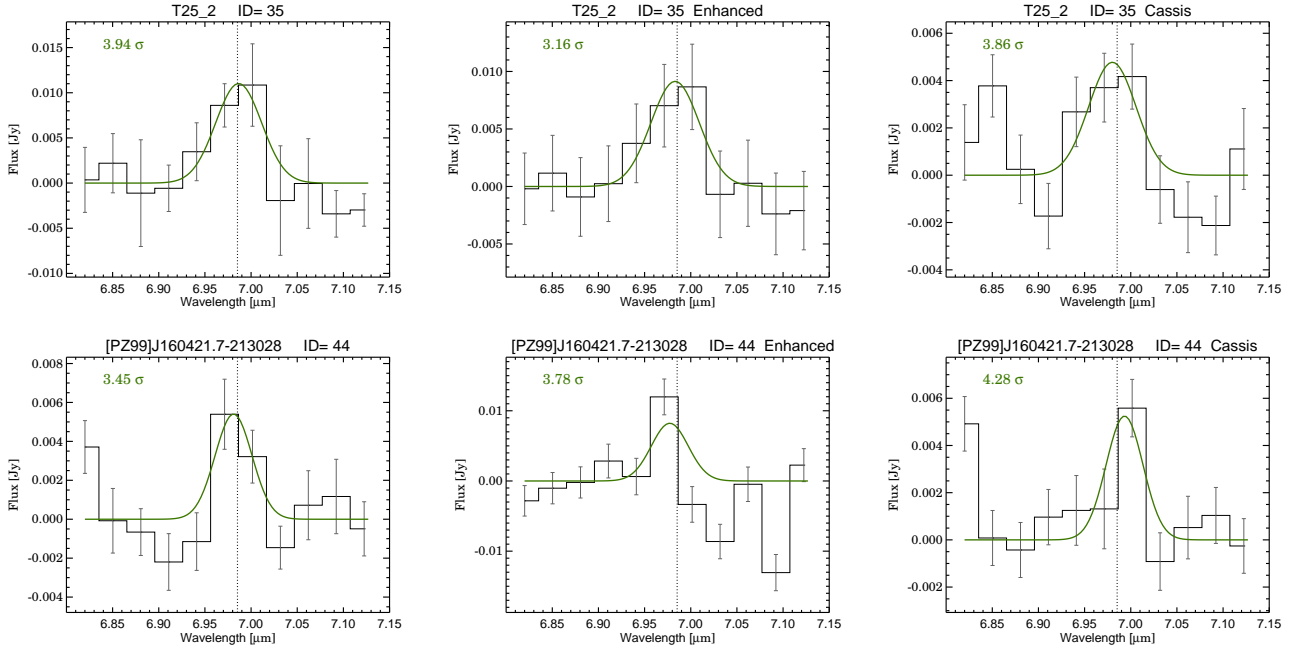


Fig. 2.— The two [Ar II] line detections with  $< 3\sigma$  level. For comparison, we plotted the same spectra reduced with different pipelines: SSC Enhanced data product in the middle, Cassis spectra at the right (see text). The green curves indicate the fitted Gaussians to the continuum-subtracted residuals. The corresponding SNR is plotted on the top left corner. The line detections are always present in the spectra regardless the used reduction pipelines.

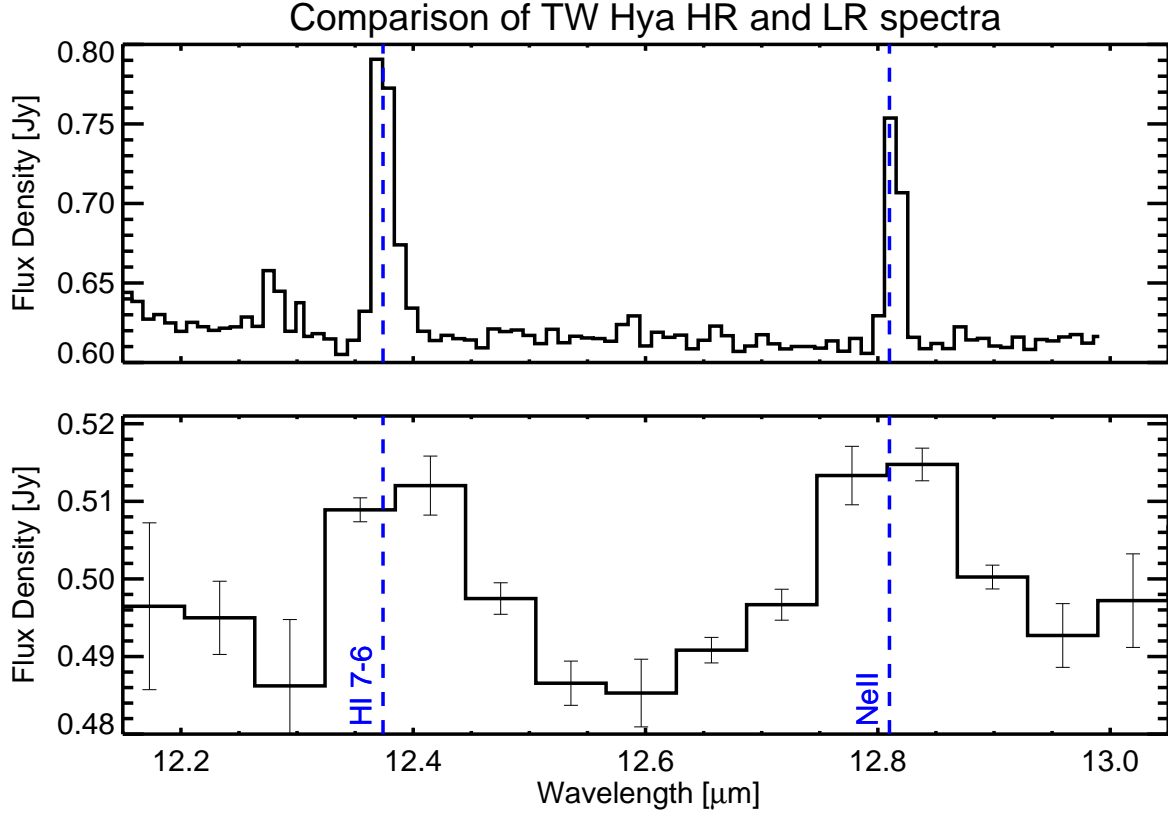


Fig. 3.— Comparison of the high-resolution (Najita et al. 2010) and the low-resolution spectrum (this paper) of TW Hya. The strongest lines are detected even in the low-resolution module. We note that the two spectra were obtained at different epochs. Hence the different line ratio of the HI(7-6) and Ne II lines could be due to source variability as already pointed out in Najita et al. (2010) for this source based on a second epoch high-resolution spectrum.

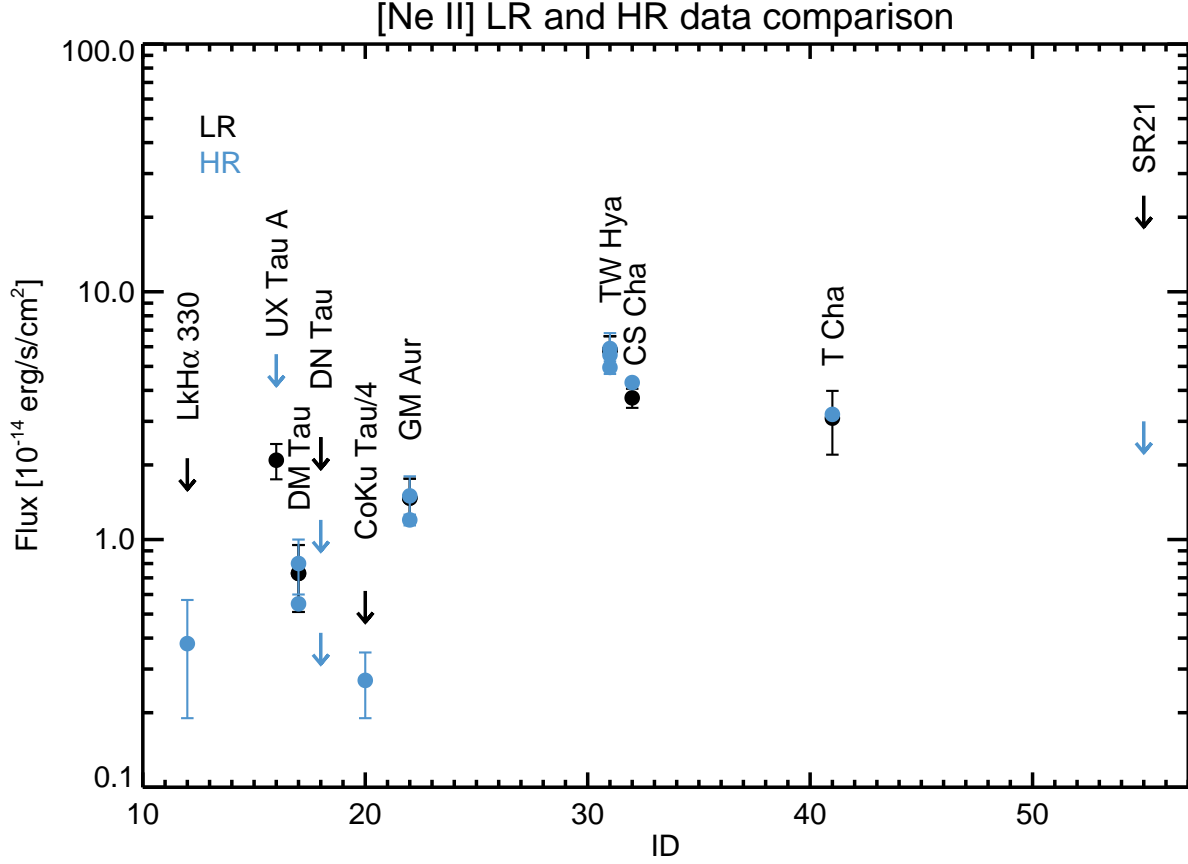


Fig. 4.— Comparison of the high-resolution (blue, Guedel et al. 2010; Najita et al. 2010; Baldwin-Saavedra et al. 2011) and the low-resolution [Ne II] fluxes (black). The low-resolution line flux values are in good agreement with the high-resolution fluxes.



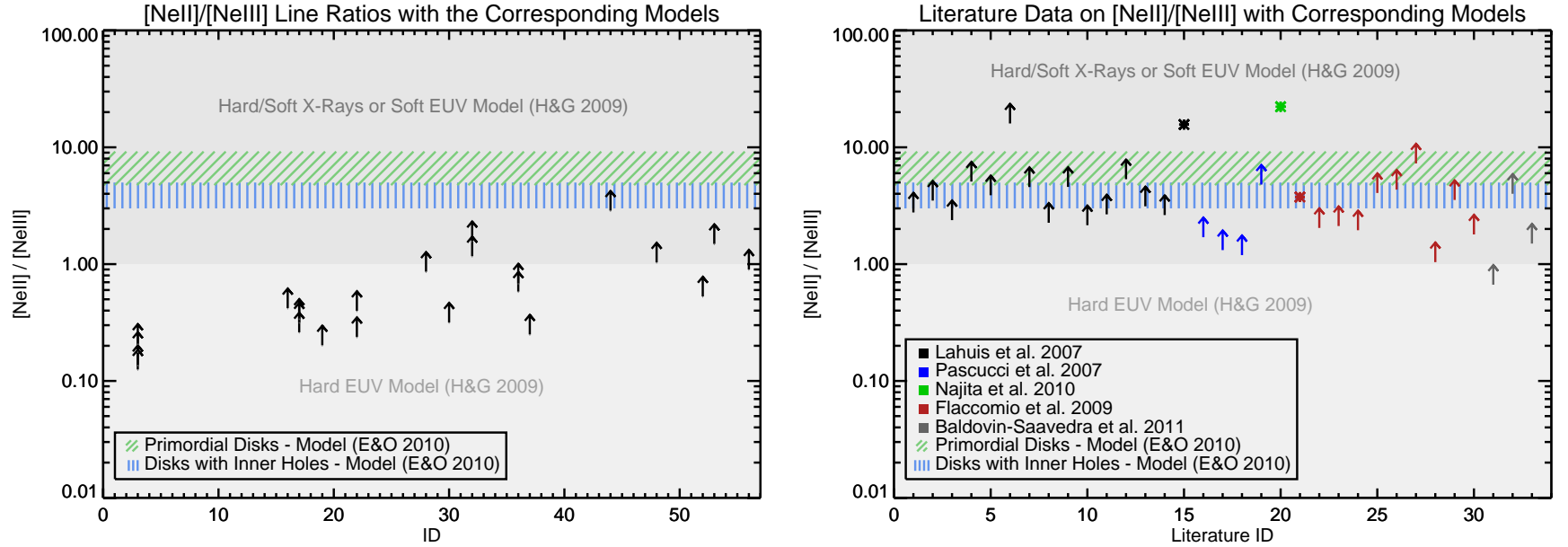


Fig. 5.— Left:  $[\text{Ne II}]/[\text{Ne III}]$  line ratios for each of the objects with  $[\text{Ne II}]$  emission. We never detected  $[\text{Ne III}]$  lines in our spectra, so all points are lower limits. Right: literature data on  $[\text{Ne II}]/[\text{Ne III}]$  line flux ratios. With darker gray background we indicate Hollenbach & Gorti (2009) model for an X-ray/soft EUV dominated stellar spectrum, while lighter gray is the hard EUV case. Note that the latter model is less likely given the distribution of lower limits. Light green slanted stripes mark Ercolano & Owen (2010) model predictions for various X-ray luminosities, while light blue straight stripes are their transitional disk models with various hole sizes. Due to the lower limits, one cannot distinguish between these different model predictions.

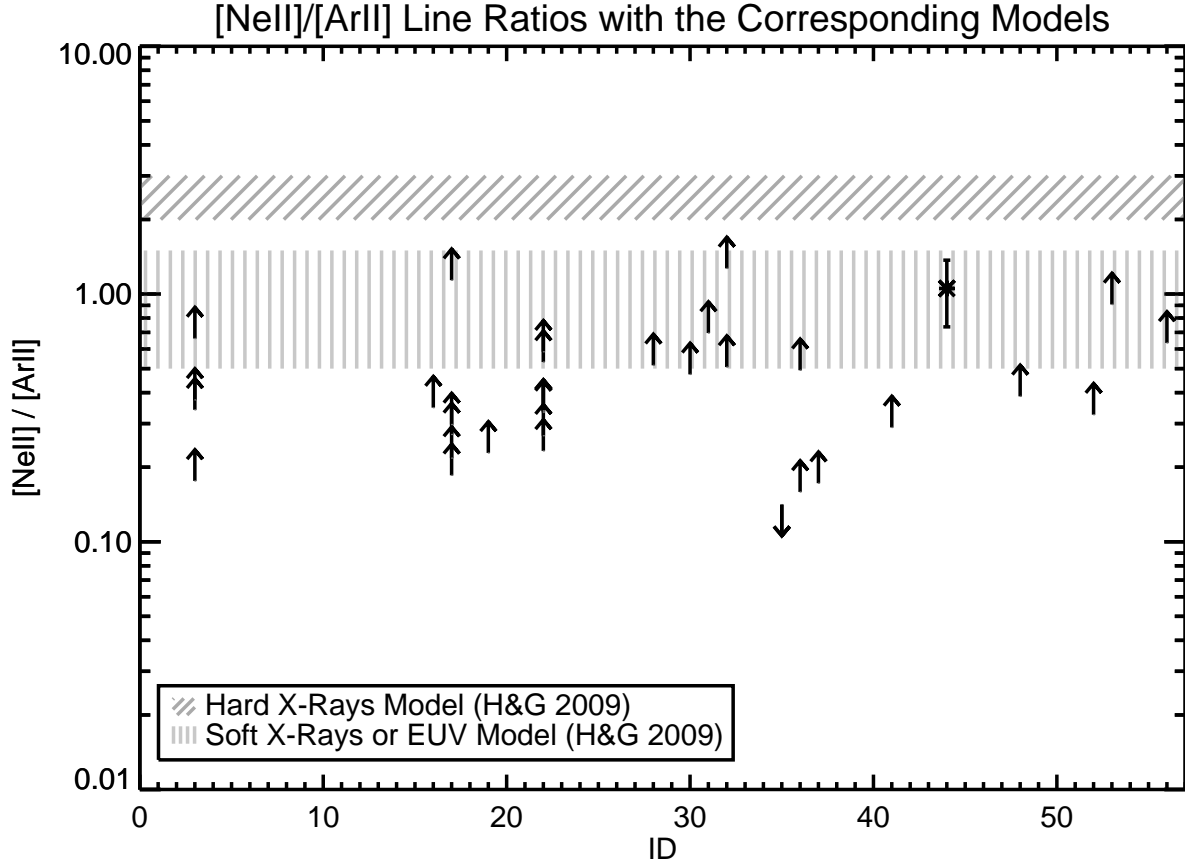


Fig. 6.—  $[\text{Ne II}]/[\text{Ar II}]$  line flux ratios for each object. We plot model predictions from Hollenbach & Gorti (2009). Light gray vertical stripes show the soft X-ray or EUV model predictions, while darker gray stripes indicate the hard X-ray model. Because of the majority of datapoints is lower limits, we cannot rule out the hard X-ray model, but the distribution hints toward to the soft X-ray or EUV model.

Table 1. The Transitional Disk Sample

ID	Source	Position ( $\alpha, \delta$ ) (J2000)	Classification Criteria	Ref.	Exposure Time (Ramp×Cycle)	AORKey
1	LAL 31	03 29 29.25 +31 18 34.7	a	1	14×13 14×3	19053312
2	SSTc2d 034227.1+314433	03 42 27.12 +31 44 32.9	b	2	14×17 30×4	19053568
3	LRL 67	03 43 44.61 +32 08 17.7	a	1	60×2 14×1	22964480
					60×2 14×1	22970624
					60×2 14×1	22970112
					60×2 14×1	22970368
					14×3 6×2	16267264
4	IC348-31	03 44 18.16 +32 04 57.0	a*,c*	3	6×2	16269056
					14×2 6×1	22963712
					14×2 6×1	22968576
					14×2 6×1	22968832
					14×2 6×1	22969088
5	IC348-44	03 44 22.57 +32 01 53.6	a*,c*	3	60×2 6×2	16266752
6	LRL 97	03 44 25.54 +32 06 17.1	a	1	14×3 30×2	16267008
7	2MASS J03443481+3156552	03 44 34.81 +31 56 55.2	b	2	14×24 14×34	19053824
8	LRL 58	03 44 38.54 +32 08 00.6	a	1	60×2 30×3	16755456
					14×3 14×2 14×1	22964224
					14×3 14×2 14×1	22966016
					60×2 none	22966272
9	IC348-133	03 44 41.73 +32 12 02.2	a*,c*	3	60×2 6×2	16266496
10	LRL 1679	03 44 52.07 +31 58 25.5	a	1	60×4 30×8	22971136
					60×3 60×4 30×4	22970880
					60×4 30×8	22971392
					60×3 30×4	22964992
11	IC348-114	03 44 56.14 +32 09 15.2	a*,c*	3	14×2 6×1	22968832
					6×2	16269056
					14×2 6×1	22968576
					14×2 6×1	22969088
					14×2 6×1	22963712
12	LkH $\alpha$ 330	03 45 48.28 +32 24 11.8	b	4	14×1	5634816
13	CX Tau	04 14 47.86 +26 48 11.0	c	5	6×1	3534592

Table 1—Continued

ID	Source	Position ( $\alpha, \delta$ ) (J2000)	Classification Criteria	Ref.	Exposure Time (Ramp×Cycle)	AORKey
14	FO Tau A	04 14 49.28 +28 12 30.5	c	5	6×1	3534592
15	FQ Tau	04 19 12.81 +28 29 33.0	c	5	14×2 14×1	3551744
16	UX Tau A	04 30 03.99 +18 13 49.3	a	6	6×1	26140928
					6×1	3536384
					6×1	27187456
17	DM Tau	04 33 48.71 +18 10 09.9	a	6	60×4 14×1	16346624
					6×4 none	15117824
					6×4 none	15117312
					6×4 none	15117568
					6×4 none	19489024
					6×4 none	19488768
					6×4 none	19488512
					6×4 none	15110912
					6×1	3536384
					6×3 6×1	26141952
					6×3 6×1	27184640
18	DN Tau	04 35 27.37 +24 14 58.9	c	5	6×1	3537152
19	LkCa 15	04 39 17.79 +22 21 03.4	b	7	6×1	3537664
					6×1	26140672
					6×1	27186176
20	CoKu Tau/4	04 41 16.81 +28 40 00.0	a	6	14×2 6×1	3548416
21	GO Tau	04 43 03.09 +25 20 18.7	c	5	6×1 14×1	3548928
22	GM Aur	04 55 10.98 +30 21 59.5	a	6	6×4 none	15118848
					6×3 6×1	27186688
					6×1	3538944
					6×4 none	15119104
					6×4 none	15119360
					6×4 none	19483904
					6×4 none	19483648
					6×4 none	19483136
					6×4 none	15111168

Table 1—Continued

ID	Source	Position ( $\alpha, \delta$ ) (J2000)	Classification Criteria	Ref.	Exposure Time (Ramp×Cycle)	AORKey
					6×3 6×1	26141696
23	CVSO 224	05 25 46.75 +01 43 30.3	b	8	60×2 30×5	16264960
24	FM 177	05 45 41.94 -00 12 05.3	a	1	240×2 60×3 120×2	12643072
25	FM 281	05 45 53.11 -00 13 24.9	a	1	240×2 60×3 120×2	12642816
26	FM 326	05 45 56.31 +00 07 08.6	a	1	14×2 6×2	18738944
27	FM 515	05 46 11.86 +00 32 25.9	a	1	14×2 14×1 14×1	12641792
28	FM 618	05 46 22.43 -00 08 52.6	a	1	14×3 14×1 14×1	12641536
29	FM 856	05 46 44.84 +00 16 59.8	a	1	14×8 14×2	18748672
30	SZ Cha	10 58 16.77 -77 17 17.0	a	6	6×1	12696832
					6×1	27187968
					6×1	26142464
31	TWHya	11 01 51.91 -34 42 17.0	b	9	6×1 none	3571456
32	CS Cha	11 02 24.91 -77 33 35.7	a	6	14×1 6×1	12695808
					6×3 6×1	26144000
33	T21	11 06 15.41 -77 21 57.0	c	10	6×1 14×1	12696320
34	CHXR 22E	11 07 13.30 -77 43 49.8	a	11	60×2 30×16	18361344
35	T25	11 07 19.15 -76 03 04.8	a	6	14×1	12695552
					6×2	26144256
					6×2	27185152
36	T35	11 08 39.05 -77 16 04.2	a	6	6×1	27185664
					6×1	26143488
37	C7-1	11 09 42.60 -77 25 57.8	a	11	60×2 120×2	12686336
38	T54	11 12 42.68 -77 22 23.0	a	6	14×1	12695552
39	Sz45 (T56)	11 17 37.01 -77 04 38.1	c	10	6×1	26142720
					6×1	27186432
					6×1 14×1	12696064
40	HD 98800	11 22 05.30 -24 46 39.3	b,c	13	6×1 none	3571969
					6×1 none	3571968
41	T Cha	11 57 13.48 -79 21 31.3	b	4	6×1 none	12679424
42	HD 135344	15 15 48.94 -37 08 55.8	b	4	6×1 none	3580672
43	Sz 84	15 58 02.52 -37 36 02.7	b	2	14×1 30×1	5644288

Table 1—Continued

ID	Source	Position ( $\alpha, \delta$ ) (J2000)	Classification Criteria	Ref.	Exposure Time (Ramp×Cycle)	AORKey
44	[PZ99]J160421.7-213028	16 04 21.65 -21 30 28.4	c*	12	6×8 14×4 120×6 30×4	19666432
45	ScoPMS 31	16 06 21.96 -19 28 44.5	a*,c*	12	6×4 14×4 6×4	17777152
46	[PGZ2001]J160959.4-180009	16 09 59.33 -18 00 09.0	a*,c*	12	6×7 6×4 30×6 6×4	17779968
47	SSTc2d J161029.6-392215	16 10 29.55 -39 22 14.4	b	2	60×4 30×10	19051008
48	RX J1615.3-3255	16 15 20.23 -32 55 05.1	b	2	6×2	15916800
49	16126-2235	16 15 34.56 -22 42 42.1	a	6	6×1	12675072
50	SSTc2d J162245.4-243124	16 22 45.40 -24 31 23.9	b	2	14×2 30×2	15920641
51	16201-2410	16 23 09.24 -24 17 04.7	a	6	6×1	12699392
52	SSTc2d J162506.9-235050	16 25 06.9 -23 50 50	b	2	14×4 30×2	19059200
53	DoAr 21	16 26 03.01 -24 23 37.9	a	1	14×3 120×3 6×1 14×1	23162624 12698368
54	DoAr 28	16 26 47.41 -23 14 52.1	a	6	14×2 30×2	12702976
55	SR21	16 27 10.27 -24 19 12.7	a	6	6×1	12698880
56	RX J1852.3-3700	18 52 17.30 -37 00 12.0	c*	14	14×4 14×24	5200640

Note. — (a) – objects were defined as transitional disks based on their spectral slopes and near IR excess; (b) – SED modeling; (c) – SED shape; (\*) – according to this work, based on color index/SED from the literature. References: (1) Muzerolle et al. (2010); (2) Merín et al. (2010); (3) Cieza et al. (2007); (4) Brown et al. (2007); (5) Najita et al. (2007b); (6) Furlan et al. (2009); (7) Espaillat et al. (2007); (8) Espaillat et al. (2008); (9) Calvet et al. (2002); (10) Kim et al. (2009); (11) Luhman et al. (2008); (12) Dahm et al. (2009); (13) Furlan et al. (2007); (14) Pascucci et al. (2007)

Table 2. Measured Line Fluxes and 3-Sigma Upper Limits

ID	Name	[Ar II] flux and uncertainty	[Ne II] flux and uncertainty ( $10^{-14} \text{erg s}^{-1} \text{cm}^{-2}$ )	[Ne III] flux and uncertainty
1	LAL_31	< 0.49	< 0.22	< 1.26
2	SSTc2d_J034227.1+314433	< 0.85	< 0.18	< 1.14
3	LRLl_67_1	< 0.62	$0.41 \pm 0.07$	< 1.97
3	LRLl_67	< 1.40	< 0.43	< 2.81
3	LRLl_67_2	< 0.99	$0.37 \pm 0.09$	< 2.95
3	LRLl_67_3	< 1.42	$0.25 \pm 0.07$	< 1.83
3	LRLl_67_4	< 0.88	$0.30 \pm 0.04$	< 1.69
4	IC348-31_1	< 6.28	< 1.86	< 2.57
4	IC348-31_2	< 1.91	< 1.73	< 2.73
4	IC348-31_3	< 2.07	< 1.25	< 5.09
4	IC348-31_4	< 1.65	< 1.10	< 4.33
4	IC348-31_5	< 2.29	< 0.90	< 3.14
5	IC348-44	< 0.59	< 0.19	< 2.57
6	LRLl_97	< 1.23	< 1.95	< 1.25
7	2MASS_J03443481+3156552	< 0.75	< 0.15	< 0.77
8	LRLl_58_1	< 1.90	< 0.95	< 3.71
8	LRLl_58_2	< 3.44	< 1.76	< 1.62
8	LRLl_58_3	< 1.69	< 1.17	...
8	LRLl_58_4	< 1.46	< 1.15	< 1.80
9	IC348-133	< 1.36	< 0.44	< 1.57
10	LRLl_1679_1	< 0.69	< 0.12	< 0.54
10	LRLl_1679_2	< 0.92	< 0.08	< 0.65
10	LRLl_1679_3	< 0.65	< 0.13	< 0.53
10	LRLl_1679_4	< 2.71	< 0.80	< 0.54
11	IC348-114_1	< 3.40	< 1.52	< 2.17
11	IC348-114_2	< 2.49	< 1.19	< 2.42
11	IC348-114_3	< 2.14	< 1.51	< 3.14
11	IC348-114_4	< 1.82	< 0.48	< 6.29
11	IC348-114_5	< 2.81	< 0.71	< 3.84
12	LkHa_330	< 5.82	< 2.13	< 2.59
13	CX_Tau	< 8.15	< 1.41	< 5.79

Table 2—Continued

ID	Name	[Ar II] flux and uncertainty	[Ne II] flux and uncertainty ( $10^{-14}\text{erg s}^{-1} \text{ cm}^{-2}$ )	[Ne III] flux and uncertainty
14	FO_Tau	< 7.90	< 2.71	< 8.85
15	FQ_Tau	< 1.88	< 0.53	< 1.74
16	UX_Tau_A_1	< 6.01	$2.09 \pm 0.34$	< 4.98
16	UX_Tau_A_2	< 4.72	< 3.64	< 4.54
16	UX_Tau_A_3	< 8.41	< 2.33	< 3.80
17	DM_Tau_10	< 4.26	$0.79 \pm 0.22$	< 3.03
17	DM_Tau_11	< 4.32	$0.94 \pm 0.29$	< 2.76
17	DM_Tau_1	< 2.69	$0.80 \pm 0.24$	...
17	DM_Tau_2	< 0.51	$0.58 \pm 0.07$	< 1.83
17	DM_Tau_3	< 2.98	< 1.04	...
17	DM_Tau_4	< 4.26	< 0.39	...
17	DM_Tau_5	< 3.32	$0.90 \pm 0.30$	...
17	DM_Tau_6	< 1.96	< 1.12	...
17	DM_Tau_7	< 3.77	< 0.54	...
17	DM_Tau_8	< 3.68	< 0.78	...
17	DM_Tau_center	< 4.60	< 0.91	< 3.31
18	DN_Tau	< 2.58	< 2.59	< 8.46
19	LkCa_15_1	< 3.81	$0.87 \pm 0.21$	< 4.31
19	LkCa_15_2	< 5.09	< 1.31	< 4.66
19	LkCa_15_3	< 8.59	< 1.38	< 2.59
20	CoKu_Tau/4	< 3.54	< 0.62	< 4.67
21	GO_Tau	< 8.85	< 2.09	< 2.27
22	GM_Aur_10	< 4.98	$1.68 \pm 0.39$	< 4.22
22	GM_Aur_12	< 6.19	$1.44 \pm 0.37$	< 6.06
22	GM_Aur_1	< 4.96	$1.65 \pm 0.32$	...
22	GM_Aur_2	< 4.18	$1.12 \pm 0.26$	...
22	GM_Aur_3	< 3.15	< 1.16	...
22	GM_Aur_4	< 3.61	< 1.36	...
22	GM_Aur_5	< 2.79	$0.94 \pm 0.25$	...
22	GM_Aur_6	< 2.48	$1.45 \pm 0.27$	...
22	GM_Aur_8	< 2.07	$1.10 \pm 0.26$	...



Table 2—Continued

ID	Name	[Ar II] flux and uncertainty	[Ne II] flux and uncertainty ( $10^{-14} \text{erg s}^{-1} \text{cm}^{-2}$ )	[Ne III] flux and uncertainty
22	GM_Aur_9	< 5.94	< 1.98	< 4.57
23	CVSO_224	< 1.03	< 0.15	< 0.55
24	FM_177	< 0.78	< 0.15	< 0.37
25	FM_281	< 0.63	< 0.26	< 0.41
26	FM_326	< 1.42	< 0.74	< 1.69
27	FM_515	< 1.76	< 1.00	< 1.33
28	FM_618	< 1.92	$0.99 \pm 0.08$	< 1.15
29	FM_856	< 1.60	< 0.39	< 2.38
30	SZ_Cha_1	< 7.92	< 2.21	< 4.88
30	SZ_Cha_2	< 6.15	< 1.44	< 3.77
30	SZ_Cha_3	< 4.58	$2.17 \pm 0.52$	< 6.86
31	TW_Hya	< 8.35	$5.81 \pm 0.81$	...
32	CS_Cha_1	< 2.94	$3.73 \pm 0.33$	< 2.37
32	CS_cha_2	< 5.58	$2.83 \pm 0.32$	< 2.42
33	T21	< 7.17	< 2.58	< 2.13
34	CHXR22E	< 0.69	< 0.09	< 0.27
35	T25_1	< 2.09	< 0.48	< 1.26
35	T25_2	$4.25 \pm 1.08$	< 0.60	< 1.86
35	T25_3	< 4.08	< 0.66	< 1.81
36	T35	< 2.68	$1.32 \pm 0.29$	< 2.27
36	T35_2	< 8.31	$1.32 \pm 0.35$	< 1.93
37	C7-1	< 0.58	$0.10 \pm 0.02$	< 0.40
38	T54	< 3.16	< 1.02	< 1.15
39	Sz_45_1	< 6.79	< 1.60	< 2.67
39	Sz_45_2	< 5.00	< 1.50	< 2.03
39	Sz_45_3	< 5.06	< 1.59	< 1.16
40	HD_98800_2	< 10.02	< 4.33	...
40	HD_98800	< 4.88	< 5.13	...
41	T_Cha	< 10.68	$3.09 \pm 0.90$	...
42	HD_135344	< 17.81	< 6.90	...
43	Sz_84	< 2.25	< 0.98	< 1.01

Table 2—Continued

ID	Name	[Ar II] flux and uncertainty	[Ne II] flux and uncertainty ( $10^{-14}\text{erg s}^{-1}\text{ cm}^{-2}$ )	[Ne III] flux and uncertainty
44	[PZ99]J160421.7-213028	$1.69 \pm 0.49$	$1.78 \pm 0.14$	$< 0.62$
45	SCOPMS_031	$< 4.19$	$< 2.47$	$< 2.14$
46	[PGZ2001]J160959.4-180009	$< 3.15$	$< 1.13$	$< 0.92$
47	SSTc2d_J161029.6-392215	$< 0.30$	$< 0.07$	$< 0.89$
48	RXJ1615.3-3255	$< 7.69$	$2.97 \pm 0.51$	$< 2.87$
49	16126-2235	$< 11.74$	$< 1.32$	$< 3.65$
50	SSTc2d_J162245.4-243124	$< 1.18$	$< 0.72$	$< 2.04$
51	16201-2410	$< 10.90$	$< 1.53$	$< 5.85$
52	SSTc2d_J162506.9-235050	$< 2.24$	$0.73 \pm 0.15$	$< 1.38$
53	DoAr_21_1	$< 18.39$	$< 23.22$	$< 17.66$
53	DoAr_21_2	$< 17.06$	$15.48 \pm 3.01$	$< 10.39$
54	DoAr_28	$< 2.38$	$< 0.62$	$< 1.67$
55	SR21	$< 19.59$	$< 24.43$	$< 87.39$
56	RX_J1852.3-3700	$< 1.26$	$0.80 \pm 0.11$	$< 0.89$

Table 3. [Ne II]/[Ne III] Line Flux Ratio Literature Data

Literature data ID	Name	[Ne II]/[Ne III] flux ratio	Ref.
1	IRAS 03446+3254	$< 2.77$	1
2	IRAS 08267-3336	$< 3.5$	1
3	Ced 110 IRS 6	$< 2.38$	1
4	VW Cha	$< 5.09$	1
5	XX Cha	$< 3.89$	1
6	T Cha	$< 16.00$	1
7	Sz 73	$< 4.57$	1
8	IM Lup	$< 2.26$	1
9	V853 Oph	$< 4.58$	1
10	IRS 60	$< 2.15$	1
11	Haro 117	$< 2.67$	1
12	SSTc2d J182928.2+02257	$< 5.33$	1
13	EC 74	$< 3.13$	1
14	EC 92	$< 2.63$	1
15	Sz 102	$15.65 \pm 4.8$	1
16	RX J1111.7-7620	$< 1.7$	2
17	[PZ99] J161411.0-230536	$< 1.32$	2
18	RX J1842.9-3532	$< 1.19$	2
19	RX J1852.3-3700	$< 4.80$	2
20	TW Hya	$22.24 \pm 16.9$	3
21	WL5/GY246	$3.75 \pm 5.3$	4
22	DoAr25/GY17	$< 2.04$	4
23	WL12/GY111	$< 2.12$	4
24	WL10/GY211	$< 1.95$	4
25	WL20/GY240	$< 4.07$	4
26	IRS37/GY244	$< 4.34$	4
27	IRS43/GY265	$< 7.28$	4
28	IRS44/GY269	$< 1.04$	4
29	IRS45/GY273	$< 3.54$	4
30	IRS47/GY279	$< 1.80$	4
31	DM Tau	$< 0.67$	5
32	Coku Tau-4	$< 4.0$	5

Table 3—Continued

Literature data ID	Name	[Ne II]/[Ne III] flux ratio	Ref.
33	GM Aur	$< 1.5$	5

Note. — References: (1) Lahuis et al. (2007) ; (2) Pascucci et al. (2007) ; (3) Najita et al. (2010); (4) Flaccomio et al. (2009); (5) Baldovin-Saavedra et al. (2011)